DISK-RESOLVED PHOTOMETRY OF ASTEROID 162173 RYUGU OBTAINED BY HAYABUSA2 VISIBLE CAMERA ONC.

Y. Yokota[1,2], R. Honda[2], E. Tatsumi[3], D. Domingue[4], S. E. Schröder[5], M. Matsuoka[1], S. Sugita[3], T. Morota[6], S. Kameda[7], T. Kouyama[8], H. Suzuki[9], M. Yamada[10], N. Sakatani[1], C. Honda[11], M. Hayakawa[1], K. Yoshioka[3], Y. Cho[3], H. Sawada[1], [1]ISAS/JAXA, (3-1-1 Yoshino-dai, Chuo-ku, Sagamihara, Kanagawa, Japan, yokota@planeta.sci.isas.jaxa.jp). [2]Kochi Univ., Japan, [3]Univ. of Tokyo, Japan, [4]Planetary Science Institute, USA, [5]DLR, Germany, [6]Nagoya Univ., Japan. [7]Rikkyo Univ., Japan. [8]AIST, Japan, [9]Meiji Univ., Japan, [10]Chiba Inst. Tech, Japan, [11]Univ. of Aizu, Japan.

Introduction: Since June 2018, the Optical Navigation Camera (ONC) onboard Hayabusa2, has observed the C-type asteroid 162173 Ryugu at a distance below 20 km [1]. ONC consists of three cameras: ONC-T, -W1 and -W2, [2–4]. ONC-T has 7 broadband filters ranging in wavelength from 0.39–0.95 μm [2]. ONC-W1 and -W2 are wide-angle (> 65°) panchromatic cameras mainly used for optical navigation during cruise and low-altitude (< 20km) operations[3]. ONC-T and ONC-W1 are used for surface imaging operations, and their images allow us to investigate the disk-resolved photometric properties of the surface.

Hayabusa2's position is nominally fixed on the line connecting Ryugu and the Earth. Therefore, the available solar phase angle range by the narrow-angle ONC-T changes seasonally with the orbits of Earth and Ryugu around the sun. Therefore, we have to collect a large number of ONC-T images over a long period of time to cover a wide phase angle range (Table 1). However, ONC-W1 covers a wider phase angle range within a single frame during the descent operations, because of its wide field of view (Fig. 1). This work focuses on data derived from the ONC-W1 images.

Table 1. Time and ONC-T phase angle.

Time	Operation topics	Phase angle
June–July, 2018	- Arrival at Ryugu (20 km). - First multi-band observation of one rotation.	~20°
Aug.–Sep., 2018	- Observations at ~5km. - Tour observation for large phase angle.	~20° to ~40°
Sep.–Oct., 2018	- Separation of rovers - Rehearsals for touchdown	~10° to ~20°
Nov., 2018 –Jan., 2019	- Conjunction operation - Zero phase angle obs.	~0° to ~10°

Data preparation: Figure 1 shows an ONC-W1 image taken during the MINERVA II1 separation operations. The shadow of the spacecraft is seen around the zero phase angle point. As shown in the right panel, various viewing geometries (incidence angle i, emission angle e, phase angle α) are observed within a single frame. Shown in blue in the left panel are areas,

such as space, shadows, and large boulders which were excluded from the analysis. We binned the ONC-W1 image data with a 5x5 pixel box, and excluded pixels imaged at large (>75°) emission angles. Applying the calibration algorithms derived for the ONC-T 550-nm band [4], the ONC-W1 response was converted to I/F. The derived I/F is plotted (Fig. 2) as a function of phase angle.
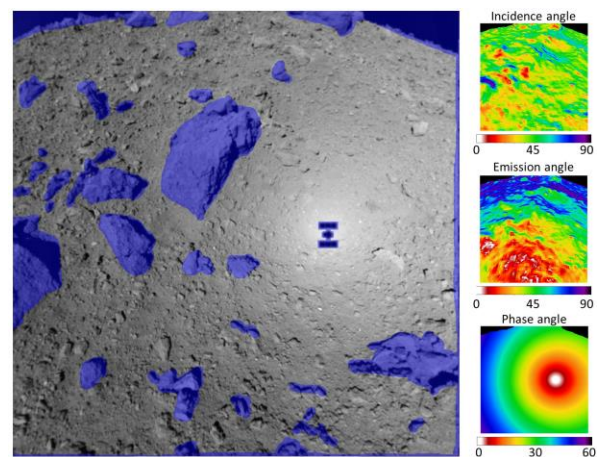

Fig. 1. (Left) ONC-W1 image (hyb2_onc_20180921_040050_w1f) acquired during decent for the MINERVA II1 release. (Right) Photometric angles of the image scene calculated from the shape model (Kobe University).
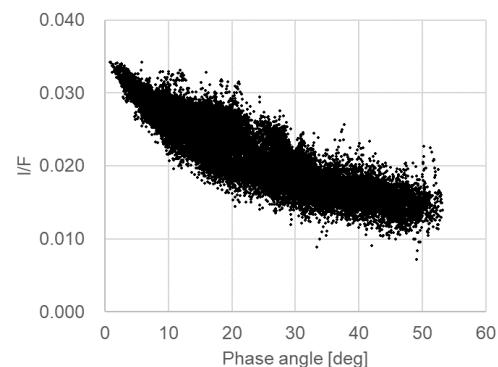

Fig. 2. I/F vs. phase angle. Multiple combinations of incidence and emission angles, for a single phase angle value, are included in the data set.

Hapke model fitting: The Hapke model equations [5 – 8] were applied to the data set using two different algorithms. The first algorithm used a least squares grid search method, which has been applied to studies of many solar system objects.. The second methodology used the MINPACK-1 least squares fitting library (MPFIT), and IDL software package. The range of Hapke parameter values are shown in Table 2.

Table 2. Hapke Model Parameter Ranges

Parameter	Range	Intermediate case
Single scattering albedo, w	0.0221 – 0.0609	0.057
Opposition amplitude, $B0$	1.0 – 8.7	1.41
Opposition width, h	0.088 – 0.286	0.138
Scattering function amplitude, b	-0.268 – -0.078	-0.225
Surface roughness, θ	27.6 – 28	28

Figure 3 plots the disk-resolved model phase curves, for the various solutions at a nadir looking condition (e=0 and i=α). This figure shows that although there was some diversity in parameter values, all solutions provide similar descriptions of the data.

The results are consistent with an intrinsically dark surface (single scattering albedo values significantly below 10%), with a surface that is rougher than the equivalently derived lunar value (20°) [9], and regolith grains that are backward scattering (as expected of dark, opaque, rough particles). The wide variation in the opposition parameters is due to the different constraints incorporated in the fitting algorithms, which need further examination.

Figure 4 plots the relationship between the opposition effect strength $B0$ and other parameters. If we restrict $B0$ to small value (≤2), then the resulting width of the opposition effect, h, is also small value (<0.2) (Fig. 4a). On the other hand, a small opposition effect leads to small b (strong back scatter) values, a mathematical compensational link in the model (Fig. 4b). Similarly, small $B0$ values lead to large w (Fig. 4c). Surface roughness θ is not sensitive to $B0$ (Fig. 4d), as expected since its properties are better determined from large incidence/emission angle data.

These modeling results, however, are in contrast to the disk-integrated values derived from fitting disk-integrated observations using Hapke's equations for disk-integrated reflectance [10,11]. The source of the inconsistency between our disk-resolved model solutions and the disk-integrated modeling results (Fig. 3) are not yet well understood. Possible sources include

calibration variations in the two data sets, photometric angle coverage between the data sets, and intrinsic differences between globally averaged data and the ONC-W1 sub-region examined.
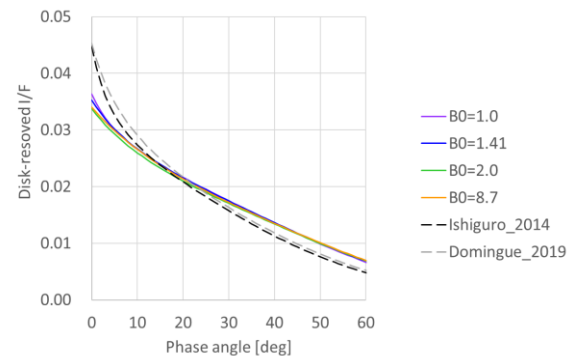

Fig. 3. Model phase curves (e=0 and i=α) from disk-resolved (solid lines) and disk-integrated (dashed lines) Hapke parameters.
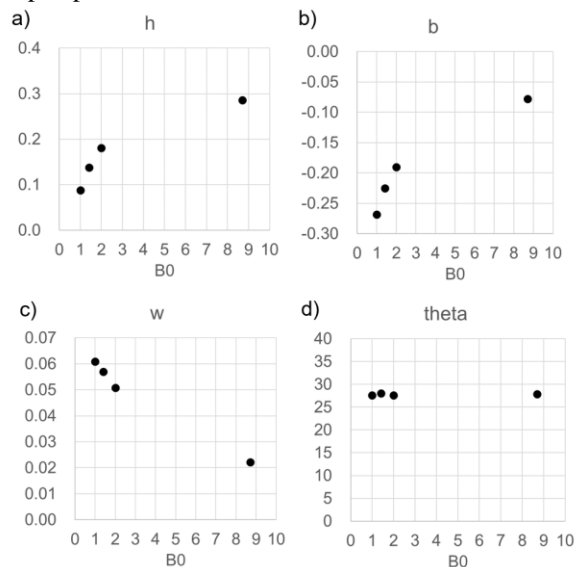

Fig. 4. Derived parameters are shown as a function of opposition effect strength $B0$. (a) Width of opposition effect, h. (b) Shape of scattering lobe, b. (c) Single scattering albedo, w. (d) Surface roughness, θ.

References: [1] Sugita et al. (submitted). [2] Kameda S. et al., 2017. *SSR* 208, 17–31. [3] Suzuki H. et al., 2018. *Icarus* 300, 341–359. [4] Tatsumi et al., (submitted). [5] Hapke, B., 1981. *JGR* 68, 4571–4586. [6] Hapke, B., 1984. *Icarus* 59, 41–59. [7] Hapke, B., 1986. *Icarus* 67, 264–280. [8] Hapke, B., 2012. Theory of Reflectance and Emittance Spectroscopy. Cambridge University Press, N.Y., 2nd Ed., 513 pp. [9] Helfenstein, P., J. Veverka 1987. *Icarus* 72, 342 – 357. [10] Ishiguro et al., 2014. *ApJ* 792, 74, [11] Domingue et al., 2019. *LPSC* 50, this issue.